

Laboratory Model Test and Numerical Analysis of Bearing Capacity of Rigid Strip Footing on Slope

Liang LU*, Katsuhiko ARAI**, Zongjian WANG* and Ryuji Nishiyama***

*Nonmember, Doctoral Program, University of Fukui (Bunkyo 3-9-1, Fukui 910-8507)

**Fellow, Dr. Eng., Prof., Dept. of Architecture and Civil Eng., University of Fukui

***Nonmember, M. Eng., Kozo-sekkei Co., LTD

This paper focuses on the estimation of bearing capacity of rigid strip footing on slope by performing a number of laboratory model tests and the numerical analysis. The laboratory model tests, including unreinforced and reinforced subsoil, are carried out using three types of subsoil. A numerical procedure is proposed which is based on a smeared shear band approach and a modified initial stress method, employing Mohr-Coulomb yield criterion with a simple plastic flow rule. The proposed procedure is capable of estimating not only the bearing capacity for natural subsoil, but also under complex conditions, for example, reinforced subsoil considering stiffness and deformation of materials. In most cases, a fairly good agreement is obtained between the experimental and analytical results.

Key Words: bearing capacity, slip surface, shear band, laboratory model test, slope

1. Introduction

When constructing structures on slope, engineers must solve complicated bearing capacity problem. Some analytical methods are available for estimating the bearing capacity on slope. The most fundamental approach is to apply the limit equilibrium method or the circular slip surface method considering the bearing capacity problem as a slope stability problem. The limit equilibrium method represents kinematical conditions only by using the mechanically acceptable shape of a slip surface, and evaluates the material properties only by its final strength. It does not allow considering the stiffness and deformation of materials, which seem to play an important role for evaluating earth reinforcement method, and which may affect the global collapse mode.

Due to these defects, some methods are proposed, for instance, finite element method, and limit analysis method which is founded on the upper and lower bound theorems in plasticity. Many researches indicate that classical finite element method does not necessarily provide a reasonable collapse mechanism^{1),2)}. Subjected to Mohr-Coulomb material, the limit analysis has not completely overcome the difficulty that the limit theorems cannot be proven without the normality rule in plasticity, and that the normality rule may not hold for the material, although it is known that the analysis provides a suitable solution in most cases despite of the difficulty. In spite

of many researches, the accurate description of localization phenomenon in soils is still open to question. For instance, the bifurcation analysis that tries to simulate actual localized deformation seems to give a promising view, while the analysis may not give reasonable solutions for complicated boundary value problems such as bearing capacity^{3),4)}. This may be because in bearing capacity problems it is not easy to duplicate the rotation of principal stresses from the below part of footing to the peripheral region. Adaptive finite element method appears to require a lot of numerical efforts and to contain a certain numerical difficulty in some cases^{5),6)}.

In recent decades, a number of analytical methods and experiments are performed to the bearing capacity problems on slope. Kusakabe et al.⁷⁾ carried out the model tests considering various factors affecting bearing capacity on slope and presented a practical solution based on the upper bound approach. They compared the solution with the results by circular slip surface method, lower bound approach, etc. Narita⁸⁾ applied the limit equilibrium analysis using log-spiral slip surface and concluded that the analysis somewhat overestimates the bearing capacity. Shields et al.⁹⁾ carried out large-scale experiments on loaded slopes of sand and compared the results with some computational results. Sugano¹⁰⁾ performed the model tests of strip footing on slope under various loading conditions and compared the result with the bearing capacity on level ground. Kimura et al.¹¹⁾ performed the

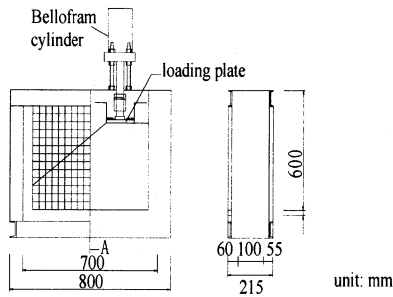


Fig. 1 Soil container

centrifuge model tests and showed a good agreement with the results of other's tests on a prototype scale. Yoo¹²⁾ and Mostafa¹³⁾ practiced the laboratory model tests and FE analysis for estimating the bearing capacity on slope reinforced by geotextile, and ascertained the accordance between the experimental and analytical results. Their main concern is the suitable distribution and properties of geotextile to establish maximum reinforcing effect rather than the simulation of ultimate bearing capacity behavior.

In this paper, laboratory model tests are carried out to evaluate the actual behavior of soil and collapse mode of soil stratum on slope under footing pressure, and to study practical evaluation of the bearing capacity. Then, we propose a numerical procedure which is based on a smeared shear band approach¹⁴⁾ and a modified initial stress method^{15), 16)}. The numerical procedure assumes Mohr-Coulomb yield criterion with a simple non-associated plastic flow rule and attempts to provide an appropriate bearing capacity which is supported by an explicit collapse mechanism represented by stress yield condition. The calculated results by the proposed procedure are compared with those obtained from the laboratory model tests, to examine the numerical characteristics and applicability of the proposed procedure.

2. Laboratory Model Test

2.1 Test Equipment

Fig. 1 shows the steel soil container used in the laboratory model test, which is 700mm wide, 100mm thick and 550mm high. One of the lateral sides has a composite glass plate with grids of 5cm size so that the deformation of subsoil can be observed obviously. Earth pressure sensors are installed in the subsoil as shown in Fig. 2, to measure the vertical earth pressure. Two dial gauges are used to measure the average settlement of loading plate. Many markers are settled on the side wall of soil container to observe the deformation of subsoil. Considering the friction between soil stratum and soil container, we use a thin rubber membrane smeared with a thin layer of silicon

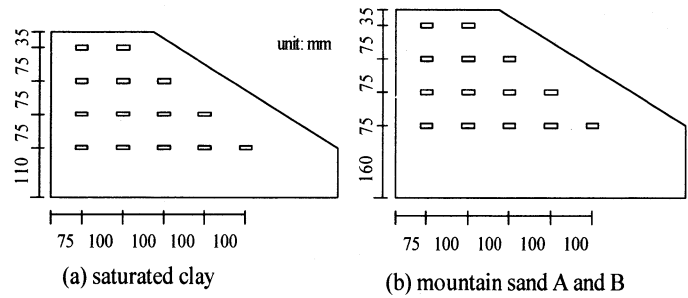


Fig. 2 Distribution of earth pressure sensor

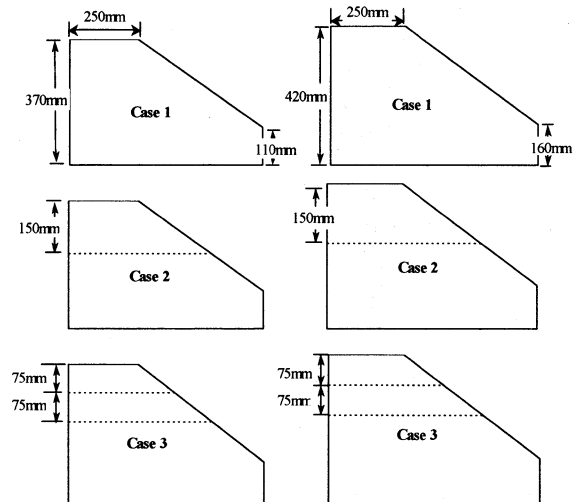


Fig. 3 Layout of geotextile for three cases

Table 1 Material properties

Soil type	saturated clay	mountain sand A	mountain sand B
B (cm)	15	15	15
c (kPa)	6.082	7.848	4.934
ϕ	0.0	15.9	27.76
E (kPa)	3924	5886	2452.5
γ (kN/m ³)	15.928	14.034	15.66
ν	0.33		
geotextile	non-woven	woven	
mass density (g/m ³)	125	130	
thickness (mm)	3.5	0.2	
strain	60%	19%	
tensile strength	90kN/m	950kN/m	
E (kPa)	9.8×10^4	4.9×10^5	

Table 2 Particle size distribution (%)

Granularity	coarse sand	fine sand	silt
mountain sand A	64.9	34.1	1.0
mountain sand B	75.5	24.0	0.5

grease on the surface of sidewalls of soil container. Loading pressure is applied to a rigid loading plate with 150mm in width using a Bellofram Cylinder. A sand paper is glued onto the undersurface of loading plate, so that it may simulate rough condition on base friction.

2.2 Soil Materials

Model tests are carried out respectively for saturated clay and two types of mountain sand. Table 1 lists the soil parameters and properties of geotextile, where B : width of loading plate, c , ϕ : Mohr-Coulomb strength parameters, E : Young's modulus, γ : unit weight and ν : Poisson's ratio. Two types of sandy soil are used and called mountain sand A and mountain sand B which particle size distribution is given in Table 2. In the model tests, c and ϕ are obtained by a direct shear test. E is back-calculated from the footing settlement observed in the model test. The model tests for discussing the effect of reinforcement material are also performed for three cases as shown in Fig. 3, where Case 1 is for the natural subsoil in which there is no reinforcement material, while Case 2 is for the reinforced subsoil with one layer of geotextile and Case 3 is for that with two layers. The placement of geotextile for each case is also illustrated by dotted lines in Fig. 3. As shown in Table 1, two sorts of geotextile are applied, non-woven and woven geotextiles corresponding to the saturated clay and the mountain sand, where E is determined by a tensile test.

2.3 Test Procedure

Foundation subsoil is made respectively of three types of soil material as shown in Table 1. For the saturated clay, clay slurry is thoroughly remoulded at water content of 65% considerably greater than the liquid limit, which is composed of sand of 17.6%, silt of 77.6% and clay of 15.3%. The clay slurry, earth pressure sensors, markers, geotextile and so on, are placed on prescribed height of soil container in turn. Note that, for each layer of setting gauge or geotextile, it is necessary to put a loading plate which has the same width and thickness as the horizontal plane of soil container. The plate is used for consolidation for one day to ensure the stable status of gauges. After setting all gauges and geotextile, the soil is put on the height a little higher than that shown in Fig. 3 (a), and then is consolidated by the way of step loads until the final pressure reaches 49kPa. Under the load steps the soil is consolidated until the completion of primary consolidation.

In terms of mountain sand, two types of sandy soil are distinguished by the density or consolidated pressure. Different from the saturated clay, which overall height is 370mm, mountain sand is put to the height of 420mm as shown in Fig. 3 (b). As above-mentioned procedure of saturated clay, the earth pressure sensors and geotextile are put into mountain sand

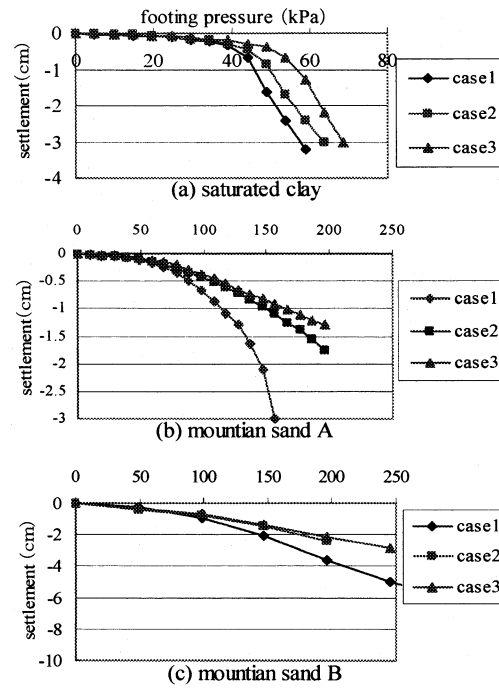


Fig. 4 Footing pressure-settlement relationship (experiment)

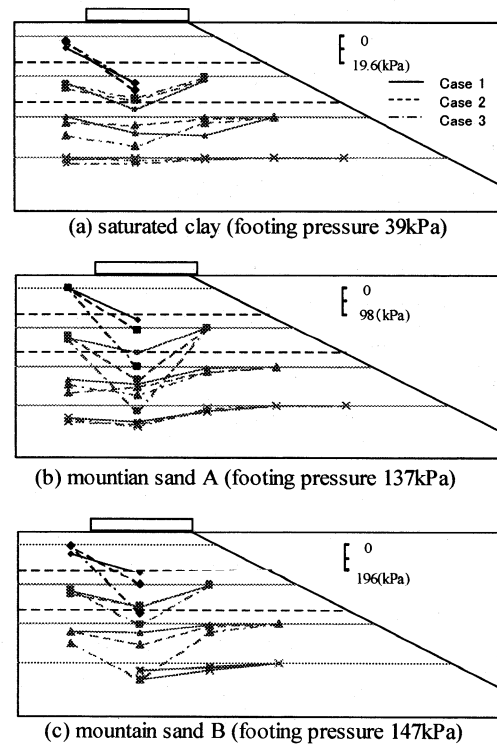


Fig. 5 Vertical earth pressure distribution (experiment)

in turn. The consolidation of mountain sand A is performed by four stepwise loads of 9.8kPa, 19.6kPa, 29.4kPa and 34.3kPa, in which each loading step is kept constant for 3 minutes for well consolidation of subsoil. For mountain sand B the loading stages of consolidation of subsoil are 24.5kPa, 49kPa, 73.5kPa and 98kPa. The first three stages are kept for 2 minutes and the final is kept constant for 5 minutes. After the subsoil has been

consolidated, the portion of subsoil near one edge is removed from the subsoil and a model slope is carefully formed.

The loading tests of saturated clay are performed by putting the loading pressure at an increment of 4.9kPa to the loading plate until the subsoil reaches failure, while mountain sand A with the increment of loading pressure of 9.8kPa and mountain sand B with 49kPa respectively. Because the soil cannot deform immediately, each loading pressure stage is stipulated to keep constant for 5 minutes. The settlement of loading plate, earth pressure of soil layer and tension of geotextile are measured at the interval of one minute until the next loading pressure stage. Photographs are taken 4 minutes after a new loading pressure is applied, in order to record the movements of the displacement markers. From these photographs, the magnitude of displacements in the slope is obtained.

2.4 Test Results

The observed footing pressure-settlement relationships are given in Fig. 4 for the three types of subsoil. As seen in Fig. 4(a), the relationships become remarkably non-linear at a certain footing pressure and may reach the bearing capacity with this turning point while tests are continued until large settlement takes place. The results of saturated clay in Fig. 4 (a) show that the earth reinforcement tends either to restrict the settlement of subsoil or to improve the bearing capacity. Compared with Case 1 of natural subsoil, in which the subsoil collapses when footing pressure reaches 44kPa, Case 2 with one layer of geotextile or Case 3 with two layers of geotextile has a higher failure load of 49kPa or 54kPa respectively. Because the placement of geotextile in Case 2 is much deeper than the region of collapse mode in Case 1 as shown later in Fig. 16 (a), the geotextile little improves bearing capacity. While the geotextile of upper layer in Case 3 largely improves bearing capacity, for its placement restricts the formation of collapse mode. Fig. 4 (b) shows the experimental results for mountain sand A. Concerning mountain sand B shown in Fig. 4 (c), the settlement is restrained by geotextile, while no clear collapse point is observed. It is difficult to evaluate quantitatively the effect of geotextile on bearing capacity for mountain sand A and B. These phenomena will be discussed later in the numerical analysis of test results. Fig. 5 shows the monitored vertical earth pressures and illustrates the comparison among three cases defined above. The figure shows that the earth pressure on the centerline of loading plate increases evidently in any instances and decreases to zero on the side of slope. For the saturated clay, near the left side of soil container the earth pressure in three cases are almost the same, except the region below geotextile. However, for mountain sand A and B, the earth pressure near lateral sidewall have a little change. The detailed discussion is made later in the numerical analysis.

3. Numerical Procedure

3.1 Outline

The proposed procedure can be used to estimate the bearing capacity directly by a development of collapse mode. The conditions to get such a collapse mode are as follows: 1) Assume an active wedge below footing, 2) Treat the yielding mass as a stratified material resulting from the smeared shear band approach, and 3) Perform rigorously the nonlinear FE analysis based on the modified initial stress method¹⁷⁾. The proposed procedure employs a simple constitutive model which requires a small number of material parameters, so that it may be applied to practical design work.

3.2 Yield Criterion

To relate the proposed procedure to conventional stability analysis, Mohr-Coulomb and Coulomb yield criteria are employed respectively to plane strain soil mass and friction interface between structure and soil. For the friction interface we employ the thin layer finite element as shown in Fig. 6¹⁸⁾.

Mohr-Coulomb:

$$F_M = \{(\sigma_x - \sigma_y)^2 + 4\tau_{xy}^2\}^{1/2} - \{(\sigma_x + \sigma_y) \sin\phi + 2c \cos\phi\} = 0 \quad (1)$$

Coulomb:

$$F_C = |\tau_{st}| - c - \sigma_t \tan \phi \quad (2)$$

where, σ_x , σ_y and τ_{xy} : stress components, and σ_t and τ_{st} : normal and shear stresses in friction interface as shown in Fig. 6.

3.3 Constitutive Relationship

(1) Stress-strain relationship for coulomb interface

Subjected to Coulomb interface, Fig. 7 schematically illustrates the relationship between shear stress vector $\{\tau_{st}\}$ and strain vector $\{\gamma_{st}\}$. We employ a simple non-associated flow rule or plastic potential Q_C defined as¹⁹⁾

$$Q_C = |\tau_{st}| - g \quad (3)$$

where g : a hypothetical parameter which is not cited actually, because Q_C is used only by its differential form. For the thin layer element, as shown in Fig.6, the elasto-plastic stress-strain relationship is given as¹⁵⁾

$$\{\delta\sigma\} = [D^{ep}] \{\delta\varepsilon^{ep}\} \quad (4)$$

where $\{\delta\sigma\} = \{\delta\sigma_s, \delta\sigma_b, \delta\tau_{st}\}^T$, $\{\delta\varepsilon^{ep}\} = \{\delta\varepsilon_s^{ep}, \delta\varepsilon_b^{ep}, \delta\gamma_{st}^{ep}\}^T$
 $[D^{ep}] = [D] - [D] \partial F_C / \partial \{\sigma\} \{ \partial Q_C / \partial \{\sigma\} \}^T [D] / \{ \partial F_C / \partial \{\sigma\} \}^T [D]$
 $\times \{ \partial Q_C / \partial \{\sigma\} \} = [d_{ij}]$

$d_{11} = d_{22} = C_1$, $d_{12} = d_{21} = C_2$, $d_{13} = d_{23} = d_{33} = 0$, $d_{31} = \pm C_2 \tan\phi$, $d_{32} = \pm C_1 \tan\phi$, $C_1 = E(1-\mu) / \{(1+\mu)(1-2\mu)\}$, $C_2 = E\mu / \{(1+\mu)(1-2\mu)\}$

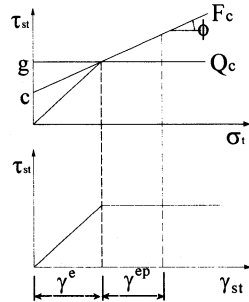
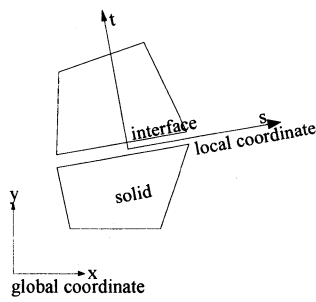


Fig. 6 Coordinates in interface element Fig. 7 Stress-strain relationship

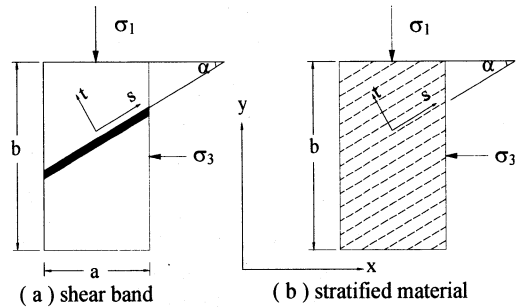


Fig. 8 Shear band formation

where $\{\delta\sigma\}$ and $\{\delta\epsilon^{ep}\}$: stress and elasto-plastic strain increments (see Fig. 7), $[D^{ep}]$ and $[D]$: elasto-plastic and elastic stress-strain matrix referred to coordinate s - t here, and d_{ij} : component of $[D^{ep}]$.

(2) Stress-strain relationship for Mohr-Coulomb material

When shearing a finite size of soil element, it is well known that we often observe a shear band or slip surface as shown in Fig. 8 (a). In this paper, the term 'shear band' is used as the meaning of a slip surface occurred in the yield element. Since our main concern is to get a practical design procedure, we employ the most fundamental expression of inclination of angle of shear band as

$$\alpha = \pi/4 + \phi/2 \tag{5}$$

Pietruszczak et al.¹⁴⁾ proposed the smeared shear band approach which evaluated the average stress-strain response of solid and shear band. When the thickness of shear band exceeds a certain thickness, the yield plane strain element becomes close to the stratified or cross-anisotropic material, as shown in Fig. 8 (b). Modified this smeared shear band approach and combined a plastic stress-strain relationship with a simple plastic flow rule as shown in Fig. 7 for Mohr-Coulomb soil mass, to get a collapse mode analogous to Fig. 10, the proposed procedure assumes the yield soil element as a stratified element and considers its elasto-plastic matrix $[D^{ep}]$ to be equal to that as given by Eq. (4).

(3) Selection of shear band

Generally a set of two shear bands or slip surfaces A - A' and B - B' are possible for a finite soil element according to the principal stress state as shown in Fig. 9 (a). Considering the formation of active wedge, we assume the shear band B - B' defined in Fig. 9 (a) within the active wedge in Fig. 10, and assume the shear band A - A' outside of the active wedge as seen in Fig. 10. The direction of A - A' or B - B' line in Fig. 9 (a) is generally determined as (see Fig. 9 (b))

$$\begin{aligned} \beta &= -\alpha - \theta && : A-A' \text{ line} \\ &= \alpha - \theta && : B-B' \text{ line} \end{aligned} \tag{6}$$

where β : inclination angle of shear band from horizontal axis,

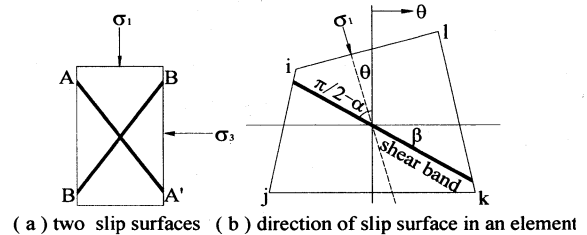


Fig. 9 Direction of shear band

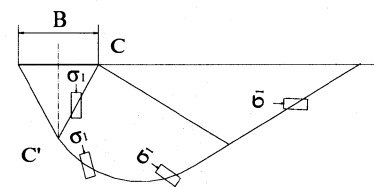


Fig. 10 Isolation of slip surface

and θ : angle of the major principal stress from vertical axis. Note that compressive stress is positive here and that shear stress τ_{st} is negative along A - A' line in Fig. 9 (a) and positive along B - B' line.

3.4 Definition of Loading State

As stated above, a stress state is assumed to move along the yield surface after yielding. The linear stress-strain relationship also happens to make the shear stress τ_{st} decrease in Fig. 7 when applying the relationship to a boundary value problem. Such a movement sometimes produces exceedingly high tensile stress for some finite elements²⁰⁾. To avoid this confusion, we introduce a constraint with respect to σ_t , which compels a stress state to move along right side in Fig. 7.

$$\delta\sigma_t \geq 0 \tag{7}$$

Eq. (7) means that normal stress perpendicular to the slip surface never decreases. The finite element, in which stresses violate Eq. (7), is called *tensile element* hereafter.

3.5 Modified Initial Stress Method

The original initial stress method is based on an iterative procedure. From mathematical viewpoint, it is a special

application of the modified Newton-Raphson method. When applying the original initial stress method together with the constitutive model described above, the numerical results are considerably affected by the finite element subdivision system, and unreasonable distributions of stress and displacement are often observed. This method treats the nonlinearity as piecewise linear, does not create the collapse mode as illustrated in Fig. 10, even though assuming the stratified material. These difficulties are avoided by introducing a modified initial stress method, which finds directly the initial stresses without iterative procedure. Fig. 11 (a) defines the actual stress of initial state $\{\sigma_I\}$, yield stress $\{\sigma_A\}$, actual stress of plastic equilibrium state $\{\sigma_B\}$, elastic stress $\{\sigma_E\}$, virtual initial stress $\{\sigma_0\}$, total strain $\{\varepsilon\}$, elastic strain $\{\varepsilon^e\}$, and elasto-plastic strain $\{\varepsilon^{ep}\}$. Yield stress $\{\sigma_A\}$ is isolated by Nayak et al¹⁶. To determine the direction of shear band, the major principal stress θ is determined by using yield stress $\{\sigma_A\}$, and use it throughout the succeeding loading stages, because the other methods do not necessarily provide a collapse mode as shown in Fig. 10.

Firstly initial stress vector in s-t coordinate is

$$\{\sigma_{s0}\} = \{\sigma_{s0}, \sigma_{t0}, \tau_{s0}\} \quad (8)$$

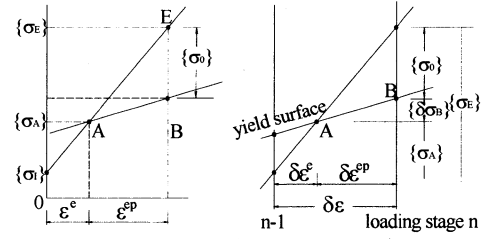
Referring to Eq. (4), component d_{ij} in $[D^{ep}]$ is the same as the component of elastic matrix $[D]$ except the third row components. This means that both σ_{s0} and σ_{t0} in Eq. (8) vanish both in interface and plane strain yield elements. The application of Eq. (8) reduces the numerical effort and clarifies the mechanical meaning of initial stresses. Referring to Fig. 11 (b), in which the stress state has attained to yield state at the present loading stage, the basic equation in the initial stress method is given as

$$\begin{aligned} \{r\}_i &= \{\sigma_{s0}\}_i - [T]_i^{-1} \{ \{\sigma_E\}_i - (\{\sigma_A\}_i + \delta \{\sigma_B\}_i) \} \\ &= \{0, 0, \tau_{s0}\}_i - [T]_i^{-1} ([D]_i - [D^{ep}]_i) ([B]_i \{ [K]^{-1} (\{\delta f\} \\ &+ \sum_j [B]_j^T [T]_j \{\sigma_{s0}\}_j A_j) \}_i - \delta \{\varepsilon^e\}_i) = 0 \end{aligned} \quad (9)$$

where, $\{\sigma_E\} = \{\sigma\}^{n-1} + [D] [B] \{\delta u\}$, $\{r\}_i$: residual, $[B]_i$: matrix for calculating strain components from nodal displacements, $[K]$: global stiffness matrix, $\{\delta f\}$: load increment vector, A_j : area of the element, and suffixes i and j denote element number. $\delta \{\varepsilon^e\}$ in Eq. (9) and Fig. 11 is calculated as $[D]^{-1} (\{\sigma_A\} - \{\sigma\}^{n-1})$. The constraint given by Eq. (7) is represented as

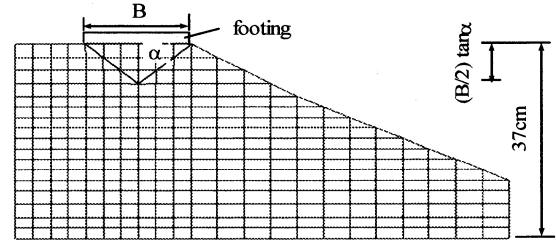
$$\begin{aligned} \{r\}_i &= \{\sigma_{s0}\}_i - [T]_i^{-1} \{ \{\sigma_B\}_i - \{\sigma_C\}_i \} = \{0, \sigma_{t0}, 0\}_i + [T]_i^{-1} [D]_i ([B]_i \\ &\{ [K]^{-1} (\{\delta f\} + \sum_j [B]_j^T [T]_j \{\sigma_{s0}\}_j A_j) \}_i - \delta \{\varepsilon^e\}_i) = 0 \end{aligned} \quad (10)$$

where $\{\sigma_C\}_i = \{\sigma_A\}_i$ or $\{\sigma_C\}_i = \{\sigma\}_i^{n-1}$ respectively when the element has yielded at the present loading stage n or when the element yielded at the preceding stage. Since both Eqs. (9) and (10) are linear equations with respect to unknown $\{\sigma_{s0}\}$, it is possible to directly solve Eqs. (9) and (10) as a set of simultaneous equations. For instance, Eq. (9) for finite element i

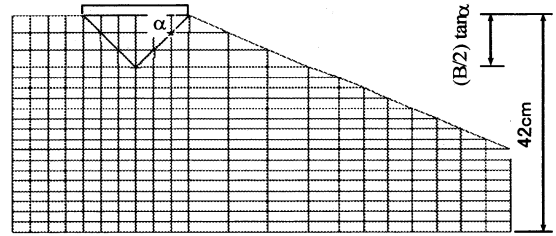


(a) initial stress method (b) initial stress method at a loading stage

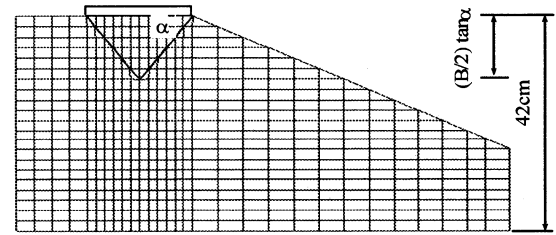
Fig. 11 Modified initial stress method



(a) saturated clay ($\phi=0$)



(b) mountain sand A ($\phi=15.9^\circ$)



(c) mountain sand B ($\phi=27.76^\circ$)

Fig. 12 FE meshing

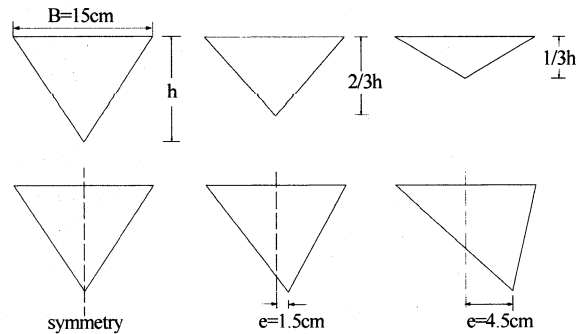


Fig. 13 Verification of shape of active wedge

with respect to unknown $\{\sigma_{s0}\}_i$ given as

$$\begin{aligned} &(\delta_{ij} - [T]_i^{-1} ([D]_i - [D^{ep}]_i) [B]_i \{ [K]^{-1} [B]_j^T [T]_j A_j \}_i \mid_3 \{0, 0, \tau_{s0}\}_i \\ &= \mid [T]_i^{-1} ([D]_i - [D^{ep}]_i) ([B]_i \{ [K]^{-1} (\{\delta f\}_i - \delta \{\varepsilon^e\}_i) \}_i \mid_3 \end{aligned} \quad (11)$$

where $| \cdot |_3$ denotes the third component of vector, etc. When solving Eqs. (9) and (10), we must assume the constant numbers both of unknown τ_{s0} and σ_{t0} . Thus the following additional iteration is required for determining the yield finite elements and tensile elements. The numerical steps during a typical loading stage are summarized as follows. 1) Performing an elastic analysis by using actual load increment $\{\delta f\}$, calculate $\{\sigma_E\}$ and $\{\delta \epsilon\}$ in Fig. 11 (b). 2) Find the yield finite elements in which $\{\sigma_E\}$ violate the yield criterion, and tensile elements in which stresses violate Eq. (7). 3) For the yield elements, calculate yield stress $\{\sigma_A\}$ both from $\{\sigma_E\}$ and the preceding stress state. 4) Concerning $\{\sigma_A\}$, calculate direction of the major principal stress θ , and find shear band inclination angle β by Eq. (6). 5) Determine $\{\sigma_{s0}\}$ by solving Eqs. (9) and (10). 6) Again, find the yield and tensile elements by performing an elastic analysis by use of both $\{\delta f\}$ and $\{\sigma_{s0}\}$ determined at 5). When finding new yield or tensile elements, determine $\{\sigma_{s0}\}$ subjected to the total yield and tensile elements including the new yield and tensile elements. Repeat this procedure until neither new yield nor tensile element is found. 7) Based on the final results at 6) calculate necessary state variables $\{\sigma_B\}$, settlements, and so on.

4. Numerical results and discussions

4.1 Preparations

The numerical procedure proposed above is applied to the laboratory model tests. Fig. 12 shows FE meshing of three sub-soils used in our analyses, in which the footing or loading plate is modeled by beam elements and represented by its elastic modulus $E=2.1 \times 10^7 \text{ kPa}$, cross area $A=0.012 \text{ m}^2$ and moment of inertia $I=1.44 \times 10^{-7} \text{ m}^4$. Interface elements as shown in Fig. 6, are set between footing and subsoil, in which shear modulus G is given as $E/2(1+\mu)$ by using E and μ of subsoil. The material parameters are given in Table 1. When considering anisotropic initial stresses, the proposed procedure provides much lower bearing capacity than conventional solutions in which anisotropic initial stresses are not taken into consideration. Thus we give isotropic initial stresses for comparing our solutions with the conventional solutions.

To get a global collapse mode, the proposed procedure requires to assume the shape of active wedge as shown in Fig. 12, because it is difficult to duplicate the rotation of principle stresses from the below part of footing to the peripheral region. Many experimental researches have observed actually the active wedge developing below footing. A lot of analyses also assumed the active wedge. For example, Kusakabe et al.⁷⁾ employs the active wedge determined by angle α similar with Eq. (5). These researches may verify the validity of the active wedge specified by Eq. (5). In our analysis,

as the first method angle α is given by Eq. (5), regarding the vertical footing pressure as the major principle stress. However, for practical design, the minimum bearing capacity must be

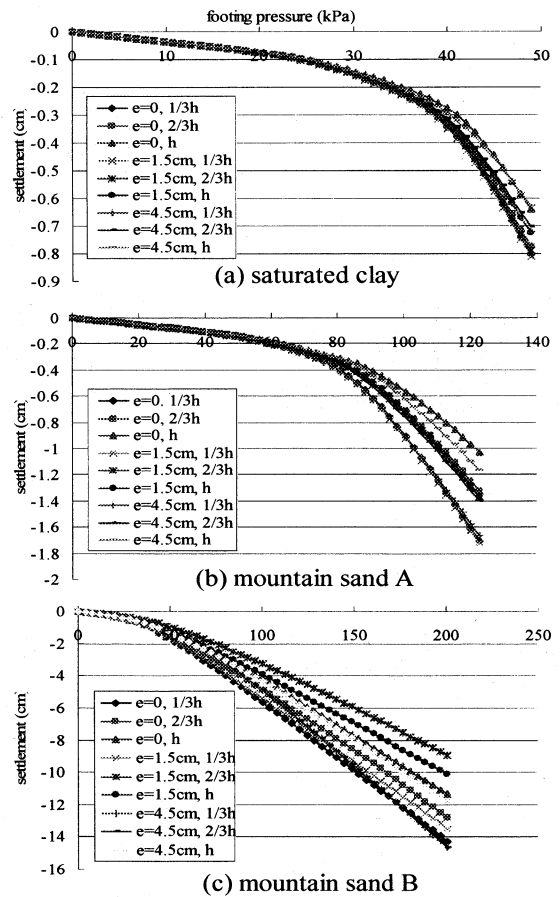


Fig. 14 Effect of shape of active wedge

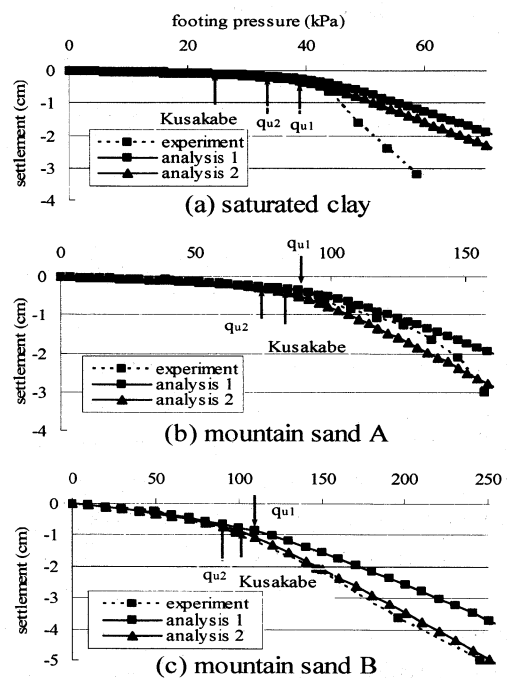


Fig. 15 Footing pressure-settlement relationship (Case 1, analysis)

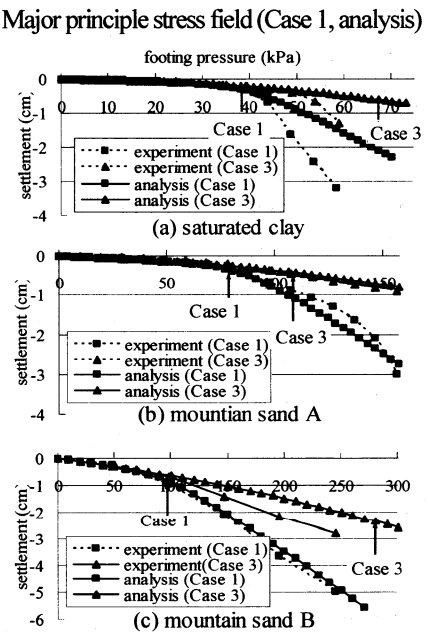
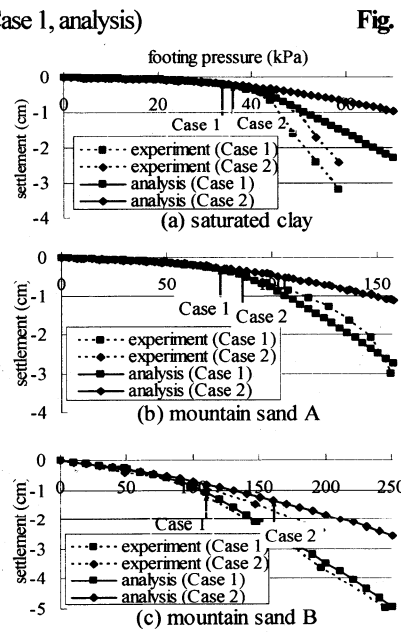
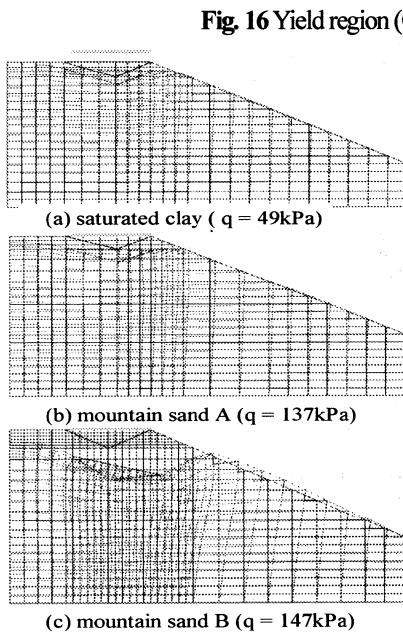
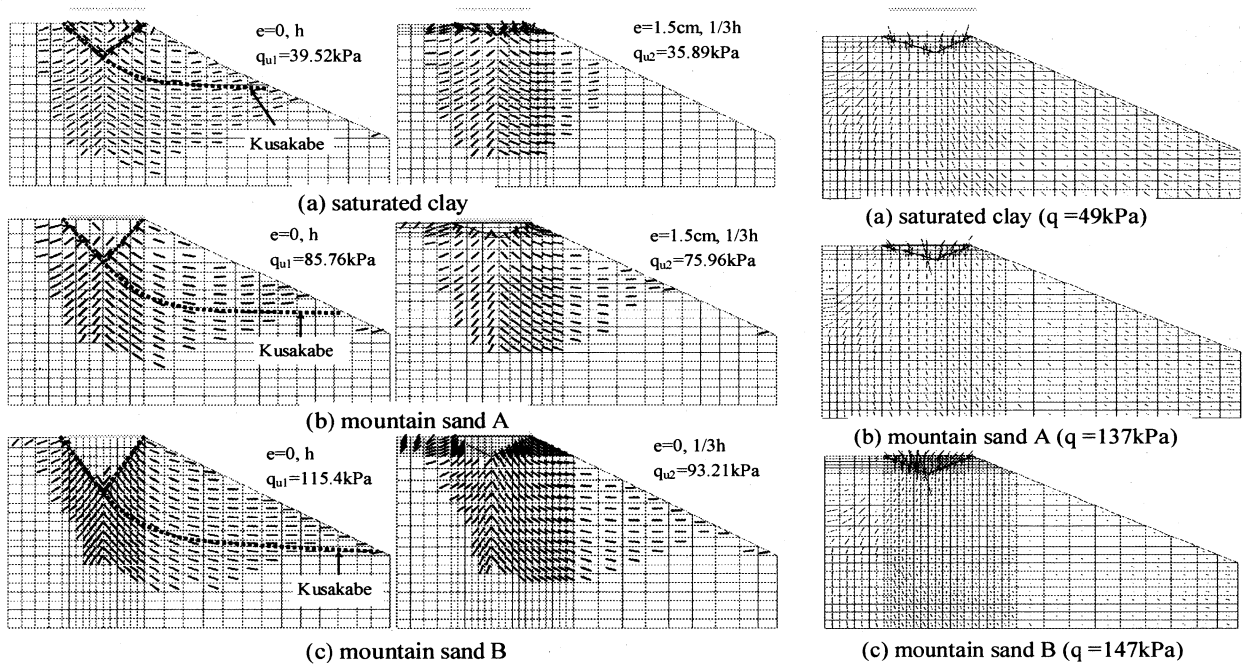


Fig. 18 Displacement field (Case 1, analysis)

Fig. 19 Footing pressure-settlement relationship (Case 2, analysis)

Fig. 20 Footing pressure-settlement relationship (Case 3, analysis)

selected by changing the shape of active wedge to ensure the bearing capacity given by the proposed procedure is conservative. In our analysis, as the second method the shape of active wedge is assumed to depend on variation of its height and eccentricity. Fig. 13 gives the patterns of active wedge assumed in our analysis. Based on the FE meshing shown in Fig. 12 with some changes for shape of active wedge in Fig. 13, the proposed procedure provides the relationship between footing pressure and settlement for Case 1 as shown in Fig. 14. It demonstrates that the calculated results are affected by the variation of active wedge in a certain extent, in which e represents the eccentricity of active wedge and h denotes the

height of active wedge as denoted in Fig. 13.

Because the proposed procedure cannot perfectly duplicate the strain localization behavior, it cannot produce an infinite plastic shear flow of subsoil. It determines the bearing capacity by the stress condition of soil mass. Because of the assumption of the smeared shear band for yield element, it may create an estimated collapse mode by the distribution of yield element. As an example, Fig. 16 shows the yield region given by the proposed procedure, where a solid line in some finite elements represents the direction of shear band or slip surface, and that these elements have yielded. Since the shear band means the slip surface in each yield element, the line connected by shear

band is thought to correspond to a continuous slip surface. It can be seen from the figure that the yield elements connect to form a collapse mode when current footing pressure reaches the denotative value. This means that the bearing capacity is determined as the value when a global collapse mode is created initially. In Fig. 16, q_{u1} represents the bearing capacity when the active wedge is determined by Eq. (5) and q_{u2} is the minimum solution of various shapes of active wedge. In this paper, we will calculate the bearing capacity for all shapes of active wedge as shown in Fig. 13, and then select the minimum solution as the bearing capacity.

4.2 Case 1 (natural subsoil)

(1) Saturated clay

The solutions calculated by the proposed procedure are compared with the results of experiments as shown in Fig. 15 (a), where the bearing capacity q_{u1} and q_{u2} are defined above and where analyses 1 and 2 correspond to q_{u1} and q_{u2} respectively. Fig. 15 contains also the upper bound solution presented by Kusakabe et al.⁷⁾ Fig. 16 (a) shows the yield region or collapse mode by the proposed procedure corresponding to the value of q_{u1} and q_{u2} . The collapse mode is supported by the principal stress field shown in Fig. 17 (a) and the displacement field shown in Fig. 18(a) which appear mechanically reasonable. Note that Figs. 17 and 18 show the result only for q_{u2} . As shown in Fig. 15 (a), the proposed procedure does not provide a clear turning point of settlement but gives the bearing capacity close to that of experiment by the way as stated before. The reason why the experimental result is slightly larger than the analytical values may be attributed to the influence of side friction between subsoil and container. The proposed procedure overestimates the bearing capacity only for the saturated clay than the solution by Kusakabe et al.

(2) Mountain sand

For two types of mountain sand, the properties are given in Table 1. As shown in Figs. 15 (b) and (c) corresponding to mountain sand A and B respectively, the bearing capacity q_{u1} and q_{u2} are defined in the same way as stated before, which depend on the collapse mode represented by the yield region as shown in Figs. 16 (b) and (c). The collapse mode is supported by the principal stress field shown in Figs. 17 (b) and (c) and the displacement field shown in Figs. 18 (b) and (c). As seen in

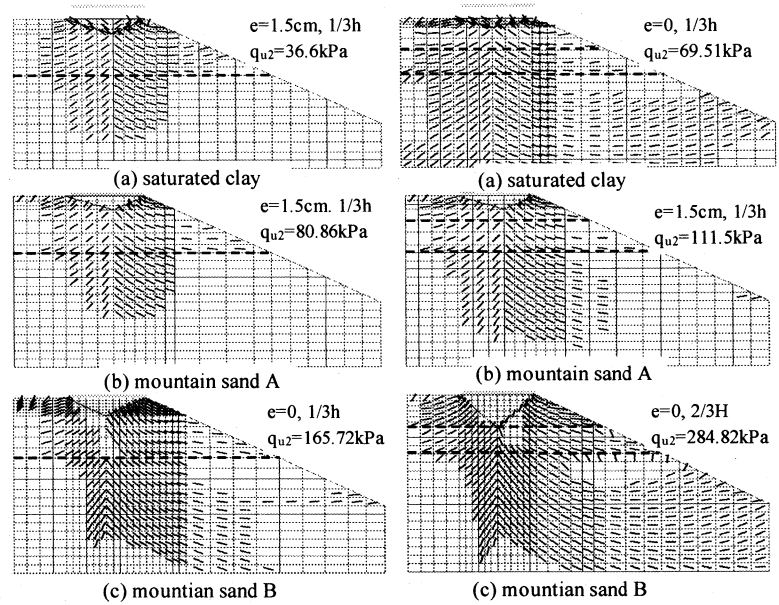


Fig. 21 Yield region (Case 2, analysis) Fig. 22 Yield region (Case 3, analysis)

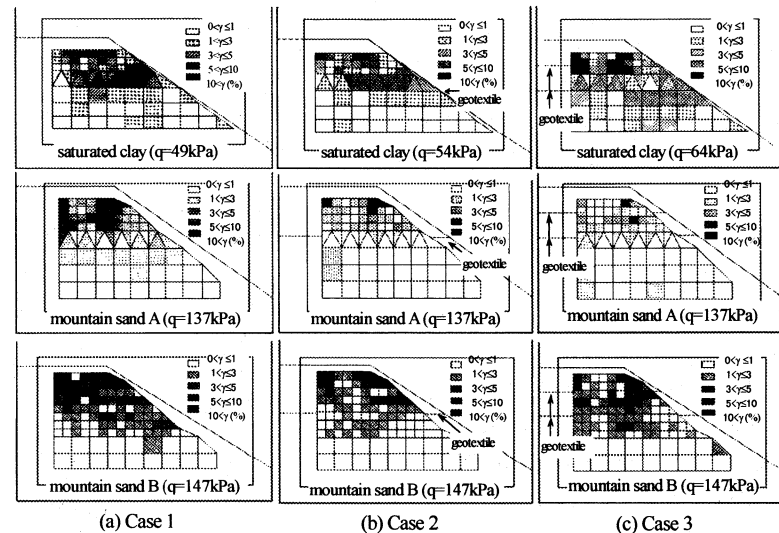


Fig. 23 Collapse mode by shear strain distribution (experiment)

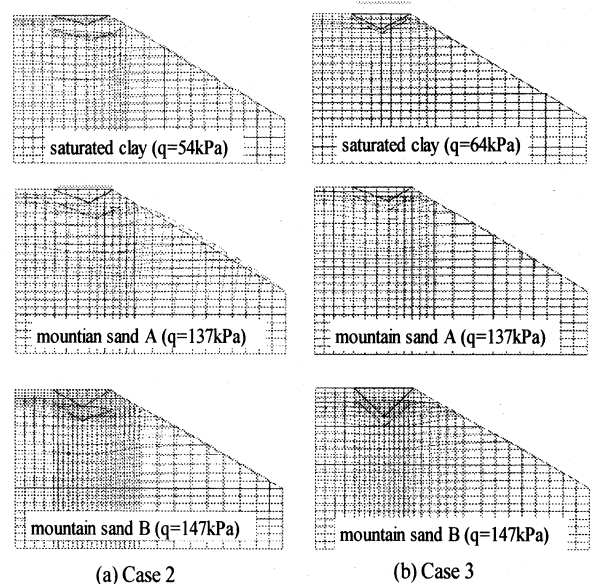


Fig. 24 Displacement field in reinforced subsoil (analysis)

Figs. 15 (b) and (c), the determined bearing capacity is in good accordance with experimental result and that by Kusakabe et al. Different from the saturated clay, the mountain sand does not form an explicit turning point of settlement both in analysis and experiment.

(3) Discussions

The collapse mode provided by the proposed procedure is created by considering the weight of subsoil, stiffness of footing and subsoil, friction between footing and subsoil, and stress concentration at the edge of rigid footing, most of which are ignored in the limit equilibrium approaches. The yield region in Fig. 16 tends to distribute more deeply below footing than that assumed in the conventional limit equilibrium analysis. This is because the vertical pressure must reach lower subsoil due to the vertical equilibrium condition, and because the pressure makes lower subsoil yield. From Fig. 18, we observe little deformation of lower subsoil. Fig. 16 shows that the collapse mode corresponding to q_{u1} is close to that by Kusakabe et al. This is because the active wedge for q_{u1} given by Eq. (5) is the same as that assumed by Kusakabe et al. However, the collapse mode for q_{u2} is shallower than that for q_{u1} . This is because the corresponding active wedge to q_{u2} is shallower than that of q_{u1} so that the obtained global collapse mode shrinks along with such an active wedge as shown in Fig. 16.

The laboratory model tests cannot provide the yield region as stated above, but it visualizes a tendency of collapse mode represented by the shear strain distribution which is calculated from the monitored displacement of subsoil. Fig. 23 shows the observed collapse mode represented by the shear strain distribution. As shown in Fig. 23 (a) the large shear strain distribute along the collapse mode shown in Fig. 16. Fig. 25 (a) shows the monitored displacement for Case 1, which gives similar tendency with the calculated displacement field shown in Fig. 18. Fig. 26 (a) compares the vertical earth pressures calculated by the proposed procedure with that monitored in the model tests. For upper subsoil the calculated earth pressure is generally in good agreement with monitored results. For lower subsoil, the calculated earth pressure is a little higher than the monitored one because the foundation subsoil is assumed to be elasto-plastic continuum in the numerical analysis.

4.3 Case 2 and Case 3 (reinforced subsoil)

(1) Saturated clay

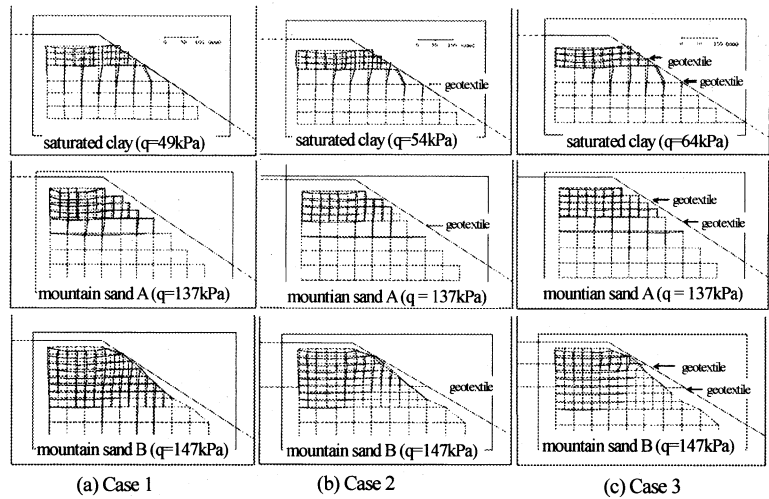


Fig. 25 Displacement field (experiment)

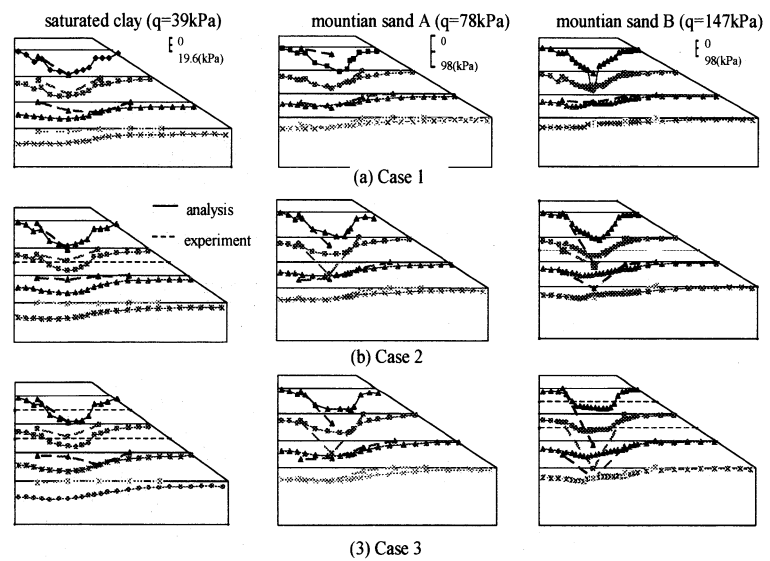


Fig. 26 Vertical earth pressure distribution

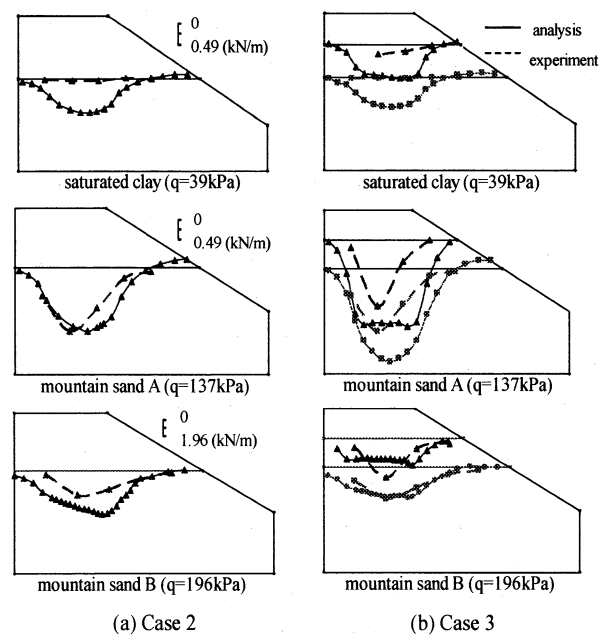


Fig. 27 Distribution of tensile force of geotextile

Figs. 19 (a) and 20 (a) illustrate the reinforcement effect on the bearing capacity in Case 2 or Case 3 comparing with Case 1 (natural subsoil). FE meshing and soil parameters are the same as those in Case 1 except the geotextile is placed as shown in Fig. 3. The properties are given in Table 1. As shown in Fig. 19 (a) for the saturated clay the reinforcement has no large improvement in Case 2. 1) The place of geotextile cannot restrict the development of collapse mode as shown in Fig. 21 (a), namely, the collapse mode is created in the upper subsoil than the location of geotextile. 2) The stiffness of non-woven geotextile used is not high. However, in Case 3 we can observe larger improvement on bearing capacity than Case 2 because the geotextile placed on the upper subsoil can effectively restrict the collapse mode as shown in Fig. 22 (a). Similar to the experimental results, the proposed procedure evaluates not only the reinforcing effect of geotextile on bearing capacity but also the restriction of settlement of foundation.

(2) Mountain sand

Figs. 19 (b), (c) and Figs. 20 (b), (c) show that the geotextile can improve the bearing capacity greatly for each of mountain sand, which agrees well with the experiment. This improvement is more evident in Case 3 than in Case 2. Such a result can be explained by the collapse mode as shown in Figs. 21 (b), (c) and Figs. 22 (b) and (c). The collapse mode is observed to be restricted to a narrow limit and to restrain the unconstrained plastic flow by geotextile especially by the upper geotextile. It is also noticeable in these figures that the geotextile of two layers restrict the development of collapse mode to a great extent. The figures show the reduction of settlement after failure of foundation for any case besides the improvement of bearing capacity. With the increase in stiffness, the controls of geotextile on settlement become clear. This tendency agrees qualitatively with the experiments.

(3) Discussions

In all cases the bearing capacity in reinforced subsoil is larger than that in natural subsoil, because the collapse mode is restricted by geotextile especially in Case 3. As seen in Figs. 21 and 22, the yield elements are mainly concentrated on the region upper the geotextile. As the experimental result, Figs. 23 (b) and (c) provide the yield region represented by the shear strain in Case 2 and 3. Compared with that in natural subsoil on the same footing pressure, the shear strain in reinforced subsoil decreases evidently for the restrained effect of geotextile. The shear strain zones in Case 2 are concentrated on the region upper the geotextile, and the largest shear strain is produced at the region below the loading plate. The trend that the shear strain in Case 3 extends widely, resembles the collapse mode created by the yield elements shown in Fig. 22. Fig. 24 shows the displacement field for these two cases. Compared with Case 1 (Fig. 18), the vertical displacement distinctly

decreases due to geotextile except for the saturated clay. The reason why the vertical displacement of saturated clay has no the distinct tendency for reinforced subsoil is due to two aspects: 1) Different loading pressure is applied to each case, while for mountain sand the same footing pressure is given. 2) Non-woven geotextile used for the saturated clay has little effect for restraining the vertical displacement. The horizontal displacements in Case 2 or Case 3 decrease evidently in all cases, particularly below the geotextile. This means that the geotextile mainly restricts horizontal displacement. The monitored vertical and lateral displacements in Fig. 25 have a fairly good agreement with the calculated those, under the footing base and on the edge of slope in most cases. Figs. 26 (b) and (c) show the vertical earth pressures in Case 2 and Case 3. In Case 2 the calculated results agree fairly well with the experimental results. In Case 3 the monitored earth pressure at centerline is considerably larger than the calculated one especially for the mountain sand, because the subsoil is particulate media which induces the concentration of stress. Fig. 27 shows the distribution of tensile force acting on geotextile. There is a little difference between the calculated and monitored results for mountain sand. This is because the stiffness of geotextile is estimated from the assumption that the stress-strain relationship is linear elastic. For the saturated clay, the large difference between them is attributed to the difficulty to evaluate the stiffness of non-woven geotextile.

5. Conclusions

This paper performed the laboratory model tests for simulating the bearing capacity of rigid strip footing on slope and proposed a numerical procedure for estimating the bearing capacity considering stiffness of material and collapse pattern. The procedure aims to fill a gap existing between conventional stability analysis and classical FEM. The procedure employs Mohr-Coulomb and Coulomb yield criteria respectively for soil mass and friction interface between soil and structure. By assuming a shear band for yield element and by employing a modified initial stress method, the procedure provides a collapse mechanism analogous to a slip surface assumed in conventional stability analysis. At the collapse mode created, a stress yield criterion is satisfied as well as along the slip surface supposed in conventional stability analysis. Such a definition of collapse mode is different from most applications of FEM which tend to express the collapse mode by the distribution of shear strain or displacement. The procedure produces a collapse mechanism as assumed in conventional stability analysis, and that the mechanism is supported by a displacement field and a stress field. This characteristic indicates the possibility of applying the procedure to the stability analysis which takes

stiffness and deformation of material into consideration.

Most case studies show that the bearing capacity obtained by the proposed procedure agrees fairly well with the laboratory model tests. These results suggest that the proposed procedure provides an appropriate solution for general problem, and that the procedure can be applied quantitatively to experimental or actual bearing capacity problems, because it requires some only fundamental soil parameters such as elastic modulus and Mohr-Coulomb strength parameters. Some case studies demonstrate that the proposed procedure can be applied to the subsoil reinforced by geotextile because it considers the stiffness and deformation of materials. The effect of reinforcement on bearing capacity is based on restricting the development of collapse mode, which leads to an increase in the bearing capacity. All the calculated results show that the earth reinforcement improves not only the bearing capacity but also the settlement after failure, which is well compatible with the monitored results. Comparisons with experimental and other analytical results show the possibility that the proposed procedure gives realistic predictions and provides a useful engineering tool for the design of foundation on slope.

REFERENCES

- 1) R. de Borst and Vermeer, PA.: Possibilities and limitations of finite elements for limit analysis, *Géotechnique*, Vol.34 (2), pp. 199-210, 1984.
- 2) Frydman, S. and Burd, HJ.: Numerical studies of bearing-capacity factor N_r , *Journal of Geotechnical and Geoenvironmental Engineering, ASCE*, Vol. 123(1), pp. 20-29, 1997.
- 3) Rundnicki, J.W. and Rice J.R.: Conditions for the localization of deformation in pressure-sensitive dilatant materials, *Journal of the Mechanics and Physics of Solids*, Vol. 23, pp.371-394, 1975.
- 4) Ortiz, M., Leroy, Y. and Needleman, A.: A finite element method for localized failure analysis, *Computer Methods in Applied Mechanics and Engineering*, Vol. 61, pp. 189-214, 1987.
- 5) Zienkiewicz, O.C. and Huang, M.: Localization problems in plasticity using finite elements with adaptive remeshing, *International Journal for Numerical and Analytical Methods in Geomechanics*, Vol. 19(2), pp. 127-148, 1995.
- 6) Hu, Y., Randolph and M. F.: Deep penetration of shallow foundations on non-homogeneous soil. *Soils and Foundations*, Vol. 38(1), pp. 241-246, 1998.
- 7) Kusakabe, O., Kimura, T. and Yamaguchi, H.: Bearing capacity of slopes under strip loads on the top surfaces, *Soils and Foundations*, Vol. 2, No. 4, pp. 29-40, 1981.
- 8) Narita, K. and Yamaguchi, H.: Bearing capacity analysis of foundations on slopes by use of log-spiral sliding surfaces, *Soils and Foundations*, Vol. 30, No. 3, pp. 144-152, 1990.
- 9) Shields, D.H., Scott, J.D., Bauer, G.E., Deschenes, J.H. and Barsvary, A.K.: Bearing capacity of foundations near slopes, *Proc. 9th ICSMFE*, Vol. 1, pp. 715-720, 1977.
- 10) Sugano, Y., Okamura, M. and Furukawa, N.: Bearing capacity and displacement characteristics of stripe foundations on slope and its application to seismic displacement prediction, *Proc. of 42nd annual symp. on the Japanese Geotechnical Society*, pp. 677-678, 2007.
- 11) Kimura, T., Kusakabe, O. and Saitoh, K.: Geotechnical model tests of bearing capacity problems in a centrifuge, *Géotechnique*, Vol. 35, No.1, pp.33-45, 1985.
- 12) Yoo, C.S.: Laboratory investigation of bearing capacity behavior of strip footing on geogrid-reinforced sand slope, *Geotextiles and Geomembranes 19*, pp. 279-298, 2001.
- 13) El Sawwaf, M.: Behavior of strip footing on geogrid-reinforced sand over a soft clay slope, *Geotextiles and Geomembranes 25*, pp. 50-60, 2007.
- 14) Pietruszczak, S. and Mroz, Z.: Finite element analysis of deformation of strain-softening materials, *International Journal for Numerical Methods in Engineering*, Vol. 17, pp. 327-334, 1981.
- 15) Zienkiewicz, O.C., Valliappan, S. and King, I.P.: Elastoplastic solutions of engineering problems 'initial stress', finite element approach, *International Journal for Numerical Methods in Engineering*, Vol. 1, pp. 75-100, 1969.
- 16) Nayak, GC. and Zienkiewicz, O.C.: Elasto-plastic stress analysis. A generalization for various constitutive relations including strain softening, *International Journal for Numerical Methods in Engineering*, Vol. 5, pp. 113-135, 1972.
- 17) LU, L., Arai, K. and Wang, Z.J.: Laboratory model test and numerical analysis of bearing capacity of rigid strip footing, *Journal of Applied Mechanics*, Vol. 10, pp. 351-362, 2007.
- 18) Desai, C. S., Zaman, M.M, Lightner, J.G and Siriwardane, H.J.: Thin-layer element for interfaces and joints, *International journal for Numerical and Analytical Methods in Geomechanics*, Vol. 8(1), pp. 19-43, 1984.
- 19) Mroz, Z.: Deformation and flow of granular materials, *Mechanics of Solids (the Rodney Hill 60th Anniversary Volume)*, pp. 119-132, Pergamon Press, Oxford, 1980.
- 20) Zinkiewicz, O.C., Valliappan, S. and King I.P.: Stress analysis of rock as a 'no tension material', *Géotechnique*, Vol. 18, pp. 56-66, 1968.

(Received April 14, 2008)